

Development of a neutraliser for air-breathing electric propulsion in very-low Earth orbit

Mansur Tisaev*[†] and Andrea Lucca Fabris*

*Surrey Space Centre

University of Surrey, Stag Hill Campus, Guildford, GU2 7XH, UK

m.tisaev@surrey.ac.uk · a.luccafabris@surrey.ac.uk

[†]Corresponding author

Abstract

A novel Air-breathing Microwave Plasma CATHode (AMPCAT) is developed to support air-breathing electric propulsion in very-low altitude orbits. In this paper, the AMPCAT plasma properties are investigated in standalone testing and compared to a hollow cathode for operation on xenon. The AMPCAT is validated through coupling with a low-power cylindrical Hall thruster (CHT), analysing both the thruster performance and plasma properties. CHT operation on xenon is sustained with the AMPCAT running on air, allowing an investigation of the influence of air as the cathode propellant and the beneficial impact of AMPCAT coupling on thruster performance recorded at low discharge voltages.

1. Introduction

The air-breathing electric propulsion (ABEP) concept refers to a spacecraft in very-low Earth orbit (VLEO), which collects rarefied upper-atmospheric air as propellant for an electric thruster. The thrust generated compensates drag at these low altitudes, around 200km, and removes the need for onboard propellant storage. This presents the opportunity of a long-duration mission in the rarely-explored VLEO regime, without the risk of leaving space debris.⁶ A long-duration spacecraft in VLEO is potentially advantageous for several mission types, such as: a) access to upper atmospheric data for scientific missions, b) a low-latency connection to ground-based users for communications spacecraft, c) an increased image resolution at a given aperture size for Earth observation satellites.¹⁹ Air-breathing spacecraft propulsion is also applicable to other bodies in our solar system, such as in the primarily hydrocarbon-based atmosphere of Mars.¹⁵ The feasibility of an ABEP system has been investigated by several previous studies,^{8,9,11,30} which typically propose a spacecraft including: a) a passive intake, which utilises the orbital speed of around 7.8km/s to collect and compress the onset airflow by a factor of $\sim 10^2$ via thermalisation, b) solar arrays for power generation, which is maximised by a dawn-dusk Sun-synchronous orbit, and c) an electric thruster downstream of the intake, ionising and accelerating particles of oxygen and nitrogen to generate thrust. Several recent ABEP studies suggest a high thruster specific impulse (I_{sp}) is needed, of at least around 3000s, due to the considerable shear drag of the solar array area required, even if these surfaces are oriented edge-on to the airflow.^{2,5,40} This suggests that a thruster based on electrostatic acceleration is suitable for an ABEP system, which requires an air-breathing neutraliser (or cathode) to support the thruster discharge.

Conventional hollow cathodes experience emitter poisoning from exposure to oxygen,^{7,13} as well as the high thermionic emission temperatures (typically $> 1000K$) causing a risk of significant cathode erosion in an oxidising environment.² As a result, a novel Air-breathing Microwave Plasma CATHode (AMPCAT) is developed within the scope of the AETHER H2020 project, which aims to design a feasible air-breathing propulsion system capable of on-ground testing in a VLEO-representative environment and provides targets for cathode performance.² The AMPCAT demonstrates an extracted current (I_{extr}) in the 1A order of magnitude when operating at a total power of roughly 130W and 0.1mg/s of a 0.48O₂ + 0.52N₂ mixture (based on expected species in VLEO).⁴¹ Standalone testing of a neutraliser prototype demonstrates stable operation at 0.8A with air on the order of several hours without any noticeable degradation, which (to the authors' best knowledge) is a first for an air-breathing cathode. Notably, the AMPCAT performance is characterised by a dual-current mode, where a higher I_{extr} is obtained above a certain bias voltage. This motivates an analysis of the internal and external cathode discharge in standalone testing, to detail the mechanisms occurring in the plasma. For operation on xenon, measurements of the external plasma parameters are also compared to a conventional hollow cathode. In order to more-properly validate the AMPCAT performance, coupled testing is performed with a cylindrical hall thruster (CHT) in the Plasma Propulsion Lab at the University of Surrey. This allows

NEUTRALISER FOR AIR-BREATHING ELECTRIC PROPULSION

an investigation into the effect of using the AMPCAT operating with xenon on both the thruster performance and plasma properties of the ion beam, in comparison to the hollow cathode reference. Subsequently, the influence on the thruster discharge of using air instead of xenon as the AMPCAT propellant is also analysed.

In a plasma cathode, ionisation of neutral propellant particles creates a discharge internal to the cathode. The internal cathode surfaces in contact with the plasma are conductive and biased at a relatively negative potential to collect a current of ions, which allows an equal electron current to be extracted from the cathode plasma while maintaining charge quasi-neutrality. This occurs over a positive potential gradient through the extraction orifice, which is imposed by the positive potential of the thruster ion beam. In the case of a Hall-effect thruster (HET), of which the CHT is an example, the cathode electron current provides: a) electrons for maintaining the ionising Hall current in the thruster channel, b) the negative electrode for the electrostatic potential gradient used to accelerate ions, and c) neutralisation of the thruster ion plume. In standalone testing, a positively-biased extracting anode is positioned downstream of the neutraliser to mimic the positive thruster potential. The relative bias between the neutraliser and extracting anode is termed V_b .

Several studies in the literature investigate the plasma properties of plasma cathodes, in particular this effort is undertaken for the $\mu 10$ microwave neutraliser developed by JAXA for the xenon-based ion thrusters of the Hayabusa missions. As in the AMPCAT, a microwave antenna is inserted directly into the plasma inside the cathode, however a key difference is the lack of an applied magnetic-field (B) in the AMPCAT design. This is unlike the $\mu 10$ neutraliser and the majority of microwave cathode literature, where the applied magnetic-field is designed to promote efficient electron heating, and so ionisation, via electron cyclotron resonance (ECR). Onodera et al³¹ find the electron temperature (T_e) inside the neutraliser is roughly constant around $2.5eV$, however T_e between the orifice and anode rises linearly up to $4eV$ with increasing V_b . This suggests a relatively low-energy electron population in the bulk internal cathode discharge, whereas external T_e increases with bias due to electron acceleration towards the anode in the cathode plume. While measuring a similar global T_e , Funaki et al¹² observe a distinct high-energy tail in the electron energy distribution function (EEDF) at increased input microwave power (P_{in}). This indicates a high degree of electron heating from oscillating magnetic and electric-fields (E) local to the plasma-immersed microwave antenna, however this degree of heating (and so a single, Maxwellian T_e) does not occur throughout the neutraliser volume. An increasing plasma (electron) density (n_e) is found generally to correspond with I_{extr} , and rises linearly with both P_{in} and cathode flow rate (\dot{m}_c) of xenon. This n_e behaviour suggests that electron extraction is to some extent impeded by the high applied $|B|$ inside the neutraliser, designed to support ECR, since a plateau in I_{extr} is observed at some conditions despite increasing electron density (and so likely ionisation) in the neutraliser plasma. This is confirmed by a later study,²⁶ and explains the detrimental magnetic confinement observed with air in AMPCAT testing and so avoidance of an applied magnetic-field in the prototype design.

Morishita et al²⁷ investigate coupling of the $\mu 10$ running on xenon with a low-power HET in comparison to a hollow cathode, enabling some comparison for this study. The authors find the thrust (F_T), specific impulse (I_{sp}) and total thruster electrical efficiency (η_T) are equivalent for the cathodes at thruster discharge current (I_d) below $0.6A$, which represents an upper limit for the microwave cathode electron emission. Beyond this the negative cathode to ground voltage (V_{cg}) of the $\mu 10$ rises sharply in order to sustain the required extracted current, which yields a penalty on the effective ion-accelerating voltage since the anode is typically biased relative to the cathode.¹⁴ Sommerville et al^{37,38} focus on the influence of hollow cathode position on a HET discharge. Notably, the authors highlight an increased plasma potential (V_s) in the thruster near-field when there is a high impedance to cathode electron motion into the ion beam. This results in a mainly-radial E-field immediately outside the thruster, which increases the beam divergence and yields a reduction in thrust.

A brief overview of CHT discharge characteristics is presented, since such a thruster is used in this study. Raitzes et al³² introduce the CHT concept as a variation of conventional annular HETs, aiming at improved performance at low discharge power (P_d) and anode flow rate (\dot{m}_a) by increasing the volume to surface ratio of the discharge channel. Ionisation occurs primarily through closed electron $E \times B$ drifts around the anode and an axial E-field, imposed perpendicular to the magnetic-field, generates downstream ion acceleration. The combination of convergence in the E-field³⁵ and a magnetic mirror formed along the thruster axis generates a high degree of electron confinement and a large density of slow ions. A significant fraction of multiply-charged xenon ions is observed in CHT testing,^{22,36} which boosts thruster performance and results in a particularly high propellant mass utilisation efficiency (η_m). Notably, the cathode electron emission is found to play a key role in the CHT discharge, with an increase in I_{extr} yielding a significant reduction in the detrimental plume divergence (that is commonly large in CHTs) and an increase in the mean ion beam energy.³³ This is explained not only by a less negative V_{cg} supporting a larger effective ion potential drop (as mentioned earlier), but via a more narrow and upstream ion acceleration region sustained by ‘extra’ cathode electrons.

The literature therefore presents a source of comparison for the AMPCAT plasma characteristics to other microwave cathodes and several potential mechanisms for the AMPCAT to display a significant impact on the CHT

discharge. The remainder of the paper is arranged as follows. Section 2 summarises the AMPCAT prototype, reference hollow cathode and CHT used in the experimental study, as well as presenting the diagnostics and setup for both standalone and coupled tests. Section 3 explores the link between AMPCAT plasma properties and extracted current in standalone testing, while Section 4 details the difference in thrust balance measurements between the two cathodes and xenon versus air as AMPCAT propellant. Finally, Section 5 compares the plasma parameters measured in the coupled CHT discharge.

2. Methodology

2.1 AMPCAT design

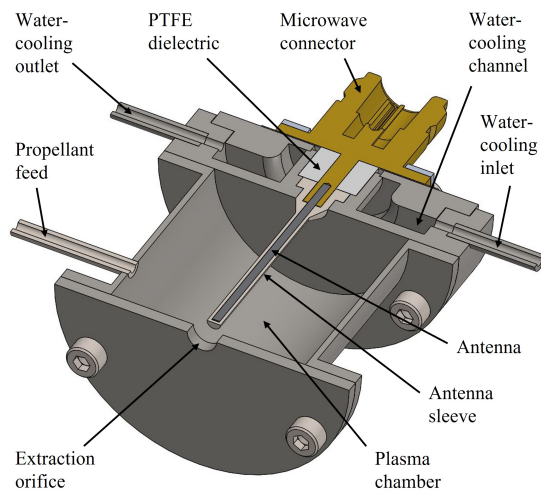


Figure 1: Cross-section of AMPCAT prototype design.

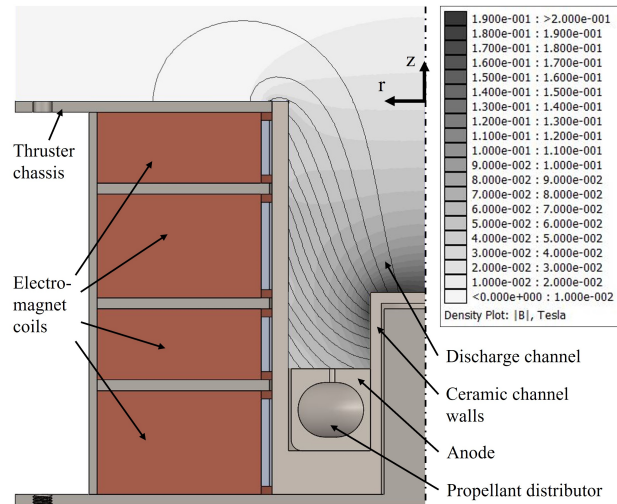


Figure 2: Axi-symmetric sectional view of CHT design with simulation of nominal B-field overlaid on discharge channel. Dashed line denotes thruster centre axis, with r and z axes also shown.

The AMPCAT prototype design is developed through iterative testing, leading to the prototype used in this study and shown in Figure 1. Neutral particles fed via the lateral inlet impinge on the high E-field expected around the tip of the antenna, as predicted by simulations of antenna-induced $|E|$ and early experimental observations.⁴¹ The time-varying electric and magnetic-fields at the $2.45GHz$ microwave frequency result in electron heating, and collisions of these high-energy electrons with neutral propellant particles form the primary ionisation mechanism of the plasma within the cathode. A negative bias is applied to the plasma-interfacing AMPCAT surfaces, allowing an ion current (I_i) to be collected within the neutraliser and an equal negative I_{extr} to be extracted along the positive potential gradient through the orifice. A current $I_i = I_{extr} = J_i A_i$ is collected, where A_i is the conducting surface area exposed to the plasma and J_i is the ion current density. The plasma-interfacing cathode surfaces are manufactured from grade 304 stainless steel due to a combination of good conductivity and resistance to oxidation at high temperatures.

A straight $\lambda/4$ microwave antenna is used for an efficient radiating length, manufactured from $1.3mm$ diameter molybdenum wire to withstand antenna heating resulting from microwave power not coupled into the plasma. Initial AMPCAT studies expose the Mo antenna surface to the air plasma, however this yields significant antenna sputtering erosion from impacts of high-energy species and the formation of a non-conductive coating on the internal surfaces, which reduces I_{extr} .⁴¹ The design is therefore updated to isolate the antenna from air plasma exposure, which is found to remove any noticeable erosion and coating while maintaining an equivalent level of extracted current. Two methods are used: a) a machined alumina sleeve with thickness in the $500 - 700\mu m$ range (as show in Figure 1), and b) an alumina plasma coating deposited on the Mo antenna to thicknesses of $100 - 300\mu m$. Neither the isolation method nor alumina thickness is found to significantly affect the cathode performance, so the isolation types are used interchangeably. The microwave connector interfacing with the antenna features a PTFE dielectric, which is seen to deform at temperatures above around $150^\circ C$, thereby reducing microwave transmission to the antenna. A water-cooling channel is therefore implemented in the AMPCAT upstream housing, allowing a stable dielectric temperature well below the identified thermal limit. Since the outer conductor of the coaxial microwave line is grounded, the microwave connector is isolated from the negatively-biased cathode surfaces with a $1.2mm$ thick Mica gasket and ceramic spacers around the fastening

NEUTRALISER FOR AIR-BREATHING ELECTRIC PROPULSION

bolts. Such a straightforward biasing approach is chosen to simplify component manufacture and assembly. The plasma chamber is sized for a sufficient A_i to sustain an extracted current in the 1A level with air, based on initial estimates of expected plasma properties. The 33mm internal diameter and nominal orifice diameter of 5mm result in a neutral density $n_n = 1.0 \times 10^{21} m^{-3}$ for air, verified without plasma using a miniature pressure sensor, and $5.0 \times 10^{20} m^{-3}$ for xenon.

2.2 Hollow cathode and CHT design

The hollow cathode used in this study as a reference is a modular design developed at the University of Surrey, intended for thruster coupling at discharge currents in the 0.5 – 4A range and at low cathode flow rates of 0.1 – 0.3mg/s with xenon. The configuration for this study is comparable to the majority of low-current hollow cathode literature, whereby a tubular BaO-W emitter (2mm inner diameter) is heated to the $\sim 1100^\circ C$ required for thermionic emission by means of a rhenium wire, threaded through a boron-nitride sleeve enclosing the emitter. A molybdenum keeper electrode is biased positively to aid electron current extraction through the 2mm diameter keeper orifice, located 2mm downstream of the emitter. Once a discharge is established, the cathode is operated in self-heating mode with the emitter surface temperature sustained by ion bombardment from the internal cathode plasma. Current-limited operation is used for the keeper, providing the required positive voltage for collection of a constant keeper current (I_k), and such an approach is used for both the standalone and coupled tests detailed in this study. A more detailed description of the cathode design and operation is presented by Ahmed et al.¹

The thruster used to investigate cathode coupling is an electromagnet version of the Halo design, an in-house Hall-effect based thruster with various configurations tested in previous research studies.^{24,42} Here, a 50mm diameter boron-nitride thruster discharge channel is used with the upstream stainless steel anode also serving as the xenon propellant feed, as shown in Figure 2. The discharge channel is composed of a short annular section of 14mm length with a 20mm diameter central piece, whereas the remainder of the channel is fully cylindrical, forming a total 50mm channel length between the anode and thruster exit plane. The magnetic circuit comprises four electromagnet coils, either 270 or 480 turns of 18 AWG enamelled aluminium wire, with inter-spacers and outer casing manufactured from ferromagnetic steel. For this study, a current of 2A is applied in the same direction for all four coils in order to generate a B-field topology as shown in the overlay of Figure 2. The thruster is therefore operated in the (non-cusp) CHT configuration commonly presented in literature,^{21,35} in order to conduct the investigation of AMPCAT coupling with a reasonably standard thruster design. In particular, a significant degree of similarity exists with the CHT studied at KAIST, which also features a 50mm diameter discharge channel and a broadly analogous B-field topology when operated with co-directed coil current, as presented by Kim et al.²⁰ The CHT's ability to maintain representative thruster performance at low discharge powers (and necessarily flow rates) is ideal for demonstrating coupled AMPCAT operation, since a thruster discharge current below 1A corresponds with the $I_{extr} = 0.5 - 0.8A$ range shown in cathode standalone testing with air.

2.3 Standalone cathode test setups

A schematic of the standalone AMPCAT configuration is shown in Figure 3a. A grade 304 stainless steel plate acts as the extracting anode and is positioned 30mm downstream of the AMPCAT orifice. The anode is biased at +20V with a DC power supply (Sorensen DLM300-2, max 600W, 300V), from which the average current is recorded as I_{extr} . A separate power supply (MagnaPower, max 2kW, 12A) applies a negative voltage to the AMPCAT body, displaying the collected ion current. It is observed that the displayed magnitudes of I_i and I_{extr} agree to within the 10mA resolution of both power supplies in nominal cathode operation. Microwave power is supplied at 2.45GHz via a coaxial N-type line (RG-393 cable) from a solid-state generator (Kuhne KUSG2.45-250A, 250W max forward power), which also measures the reflected power in the line. A DC block (MECA) is used to isolate the generator from any DC plasma current and a stub tuner (Arios, max 200W) enables impedance-matching to minimise the reflected power. Small holes are drilled in the N-type microwave connectors within the vacuum chamber to prevent connector damage from a multi-pactor breakdown due to any unevacuated air. The propellant feed and water-cooling tubes (Swagelok 1/8") are brazed to the cathode body, and isolated from the AMPCAT bias with a ceramic spacer and plastic tubing respectively. A water-chiller (R-Tech, 3bar pressure) provides the cooling flow and propellant is supplied from compressed gas bottles, via a mass flow controller for both the 0.48O₂ + 0.52N₂ air mixture (Bronkhorst El-Flow, max 200sccm Ar, precision 0.1sccm) and xenon (Bronkhorst El-Flow, max 20sccm Xe, precision 0.01sccm). The vacuum chamber for AMPCAT testing (Kurt.J.Lesker, 60×30×30cm internal dimensions) achieves a background pressure of $< 1 \times 10^{-5} mbar$ without flow according to a cold cathode ionisation gauge (Leybold PTR90, 10^{-8} to $10^3 mbar$ range). The background pressure is within a range of $2.2 - 4.8 \times 10^{-4} mbar$ and $0.7 - 1.4 \times 10^{-4} mbar$ for air and xenon respectively over the 0.05 – 0.15mg/s mass flow rates tested.

NEUTRALISER FOR AIR-BREATHING ELECTRIC PROPULSION

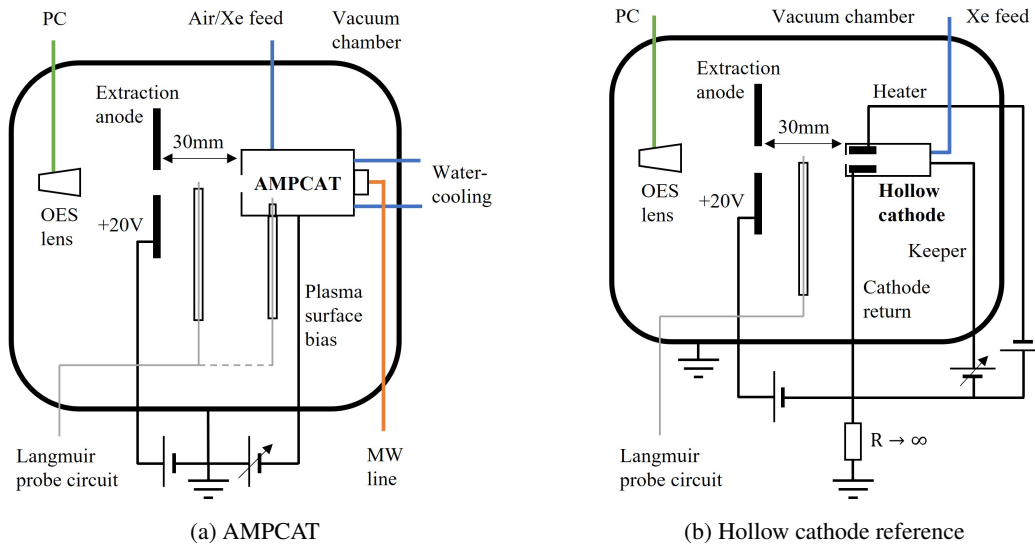


Figure 3: Schematic for plasma diagnostics of cathodes in standalone setup.

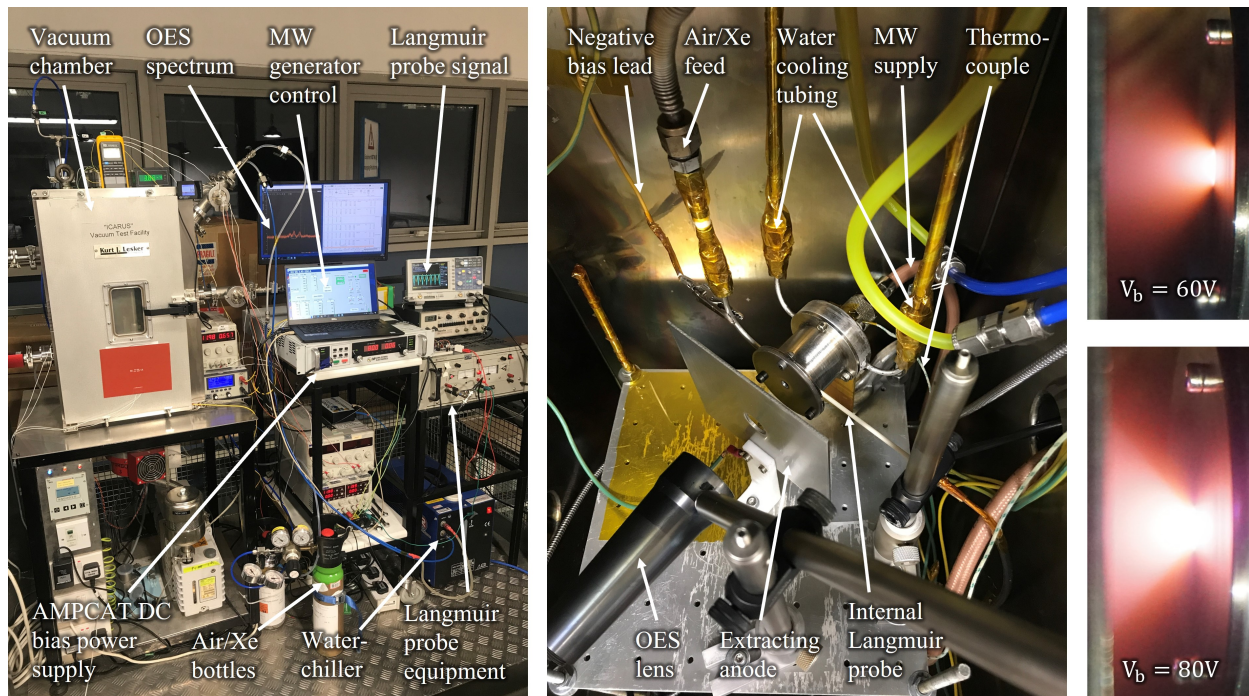


Figure 4: **Left:** Laboratory apparatus for AMPCAT, shown during standalone testing with plasma diagnostics. **Centre-right:** Feed and probe setup inside vacuum chamber. **Far-right:** AMPCAT plasma discharge in orifice-anode region, showing lower and higher- I_{extr} mode with $P_{in} = 48W$ and $\dot{m}_c = 0.1mg/s$ of $0.48O_2 + 0.52N_2$ air mixture.

As also shown in Figure 3a, the AMPCAT discharge is sampled by an internal and external single Langmuir probe, which are developed for this study. The probes utilise a $0.4mm$ diameter tungsten wire, protruding $2mm$ from an alumina tube with a gap to the bore. The external probe is positioned $15mm$ downstream from the orifice along the AMPCAT axis, halfway to the anode, and uses a $2mm$ diameter ceramic tube. Since the internal probe is immersed in the cathode plasma volume, a smaller $1.2mm$ diameter tube extends inside the AMPCAT to minimise disturbance of the plasma. The probe tip is positioned opposite to the propellant inlet, $7mm$ upstream of the orifice, and at half the radius of the cylindrical wall. A saw-tooth probe voltage ramp is supplied at $0.7Hz$ by a signal generator (Thandar TG2001), allowing an average to be taken between 6 – 7 probe acquisitions, and the probe voltage is amplified to a range of at least -50 to $50V$ by a bi-polar amplifier (KEPCO BOP-500M). The probe current is recorded over a 100Ω shunt resistor, using a difference amplifier (Analog Devices AD629) to remove the common-mode voltage and

NEUTRALISER FOR AIR-BREATHING ELECTRIC PROPULSION

an oscilloscope (RTC1002) to save at least 6×10^4 voltage and current data-points per ramp. An optical emission spectroscopy (OES) analysis is also conducted to measure the emission spectrum of the AMPCAT plasma, with a lens (Ocean Insight 84-UV-25) positioned 60mm downstream of the orifice. The lens views the internal cathode discharge through a central 15mm diameter opening in the anode plate, interfacing with a spectrometer in the near infra-red range (Ocean Insight HR4000CG-UV-NIR, $200 - 1100\text{nm}$ wavelengths). An equivalent Langmuir probe and OES setup is used for standalone testing of the hollow cathode, the schematic for which is shown in Figure 3b. The only difference is an 80mm distance between the cathode orifice and OES lens; a minor change given the broad focusing distance of the lens used. The keeper bias (Sorensen XG 300-5.6) and heater power (Sorensen DLM 40-15) are provided by DC power supplies. The equipment and setup inside the vacuum chamber for the AMPCAT standalone testing is shown in Figure 4. The visual plasma emission of the external cathode discharge when operating on air is also pictured, showing the clear transition in intensity between the lower and higher-current modes (further details in Section 3.2).

2.4 Thruster coupled test setup

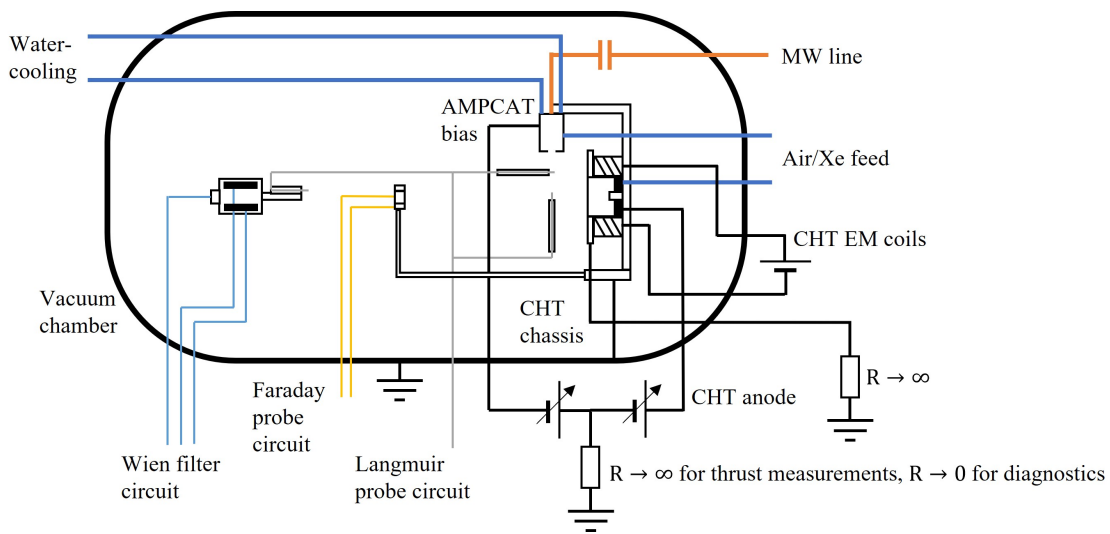


Figure 5: Schematic of setup for testing of AMPCAT coupled with CHT.

A schematic of the coupled setup for the AMPCAT coupled with the CHT is shown in Figure 5. The thruster and cathode are mounted on a torsional thrust balance with a resolution in the $\mu\text{N} - \text{mN}$ range, incorporating a microwave waveguide and liquid conductor reservoirs to avoid the stiffness of the microwave and DC cables respectively from influencing the thrust measurement. Further details on the balance are presented by Masillo et al.²⁵ The thruster chassis is electrically isolated from the grounded chamber and thrust balance (i.e. floating), whereas the anode and cathode return is grounded when using plasma diagnostics to allow a stable reference for V_s of the discharge. The cathode supplies are the same as detailed in the previous section, with additional supplies for the anode (Sorensen SGA 1000-5, max 5kW) and thruster electromagnet coils (TTi CPX200D, max 180W). Both cathodes are mounted with their orifices at a radius (r) of 65mm and axial distance (z) of 40mm from the centre of the CHT exit plane. The AMPCAT is aligned perpendicular to the thruster axis to avoid any \dot{m}_c contribution to measured thrust, while the hollow cathode is canted slightly towards the CHT channel at 20° , due to use of an existing mounting bracket. The difference in angle is expected to be negligible since the axial component of the orifice normal vector is vanishing in both cases. The respective cathode alignment with respect to the thruster and balance can be seen in Figure 6. It is verified that the AMPCAT water-cooling does not affect the linearity of the thrust balance calibration curve and multiple thrust step readings are taken for each data-point. The coupled tests are conducted within a 1.5m diameter and 3m long vacuum chamber, with a base pressure below $1.5 \times 10^{-5}\text{mbar}$ without flow and below $4.2 \times 10^{-5}\text{mbar}$ for the maximum $\dot{m}_a = 0.7\text{mg/s}$ Xe and $\dot{m}_c = 0.1\text{mg/s}$ air tested.

The plasma diagnostics used for the coupled tests are also pictured in Figure 6. These include two single Langmuir probes positioned in the CHT near-field to measure differences in V_s , T_e and n_e between the cathodes. The probe design is equivalent to that described in Section 2.3. The fixed probe locations are along the thruster axis ($z = 20\text{mm}$, $z = 40\text{mm}$ and $z = 60\text{mm}$), primarily to investigate the spatial distribution of ion-accelerating potential, and on both sides of the thruster discharge along the cathode axis ($r = 32\text{mm}$ and $r = -32\text{mm}$ at $z = 40\text{mm}$), to pick up any cathode-induced plume asymmetry. A Faraday probe mounted on a rotating arm is used to map the angular ion current

NEUTRALISER FOR AIR-BREATHING ELECTRIC PROPULSION

distribution at a radius of 375mm . The planar probe is a 20mm diameter molybdenum disc in a boron-nitride housing, with a 30mm outer diameter guard ring, biased at -30V to achieve ion saturation. A Wien filter (also known as an E×B probe) is used in order to detail the ion energy distribution, identifying the beam voltage V_B and the presence of multiply-charged ion species. The probe is positioned at $z = 600\text{mm}$ and the 1.6mm diameter collimator opening is aligned with thruster axis. In order to adjust the measured V_B for the residual plasma potential, an additional Langmuir probe is located at the collimator entry to record the local V_s . Further details on the design and operation of the Faraday probe and Wien filter are presented by Masillo at el.²⁴ Figure 7 shows the CHT discharge plasma when coupled with the AMPCAT, for: a) xenon through the cathode and thruster anode, b) AMPCAT running on air, and c) both thruster and cathode running on air. While stable thruster operation is achieved, the case of air through the anode is not discussed further since the CHT is optimised for xenon propellant.

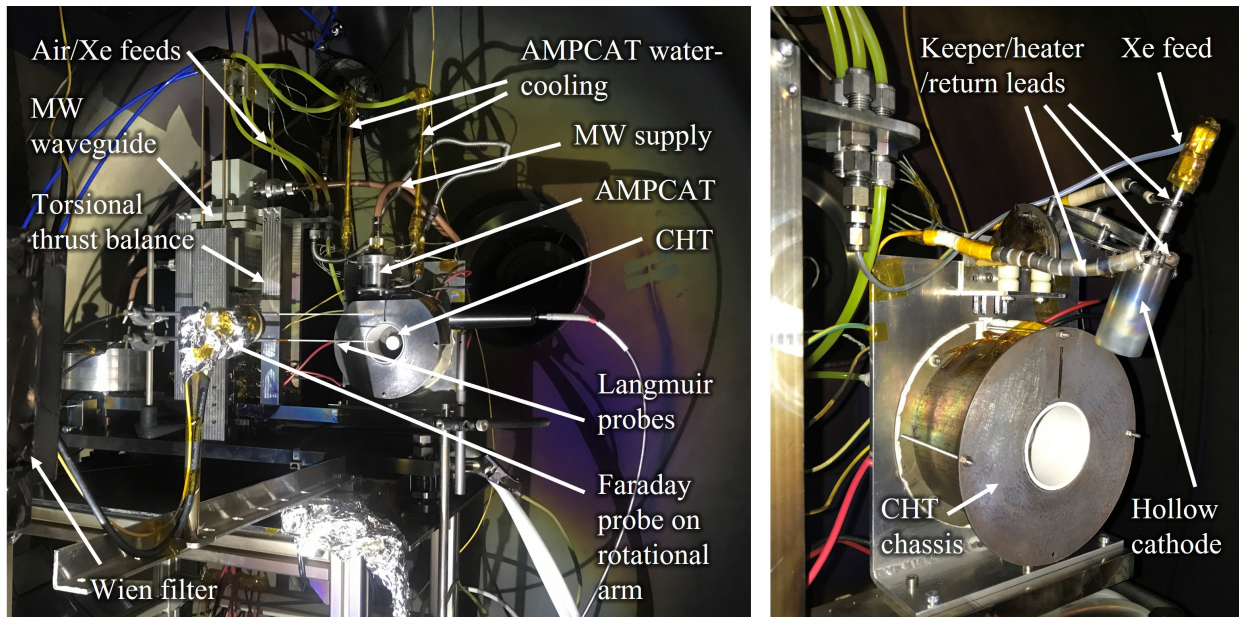


Figure 6: **Left:** Setup for plasma diagnostics tests of AMPCAT coupled with CHT inside vacuum chamber, showing probes and torsional thrust balance. **Right:** CHT coupled with hollow cathode reference on thrust balance beam.

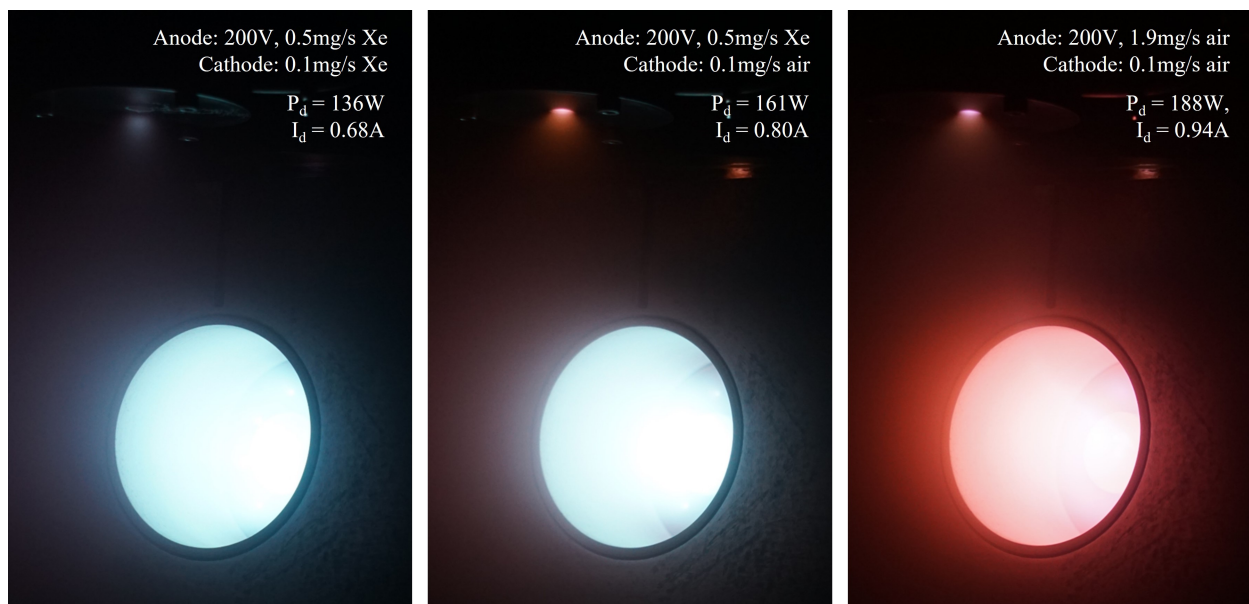


Figure 7: Thruster and cathode plume of AMPCAT coupled with CHT for varying propellant through anode and cathode. Discharge current and power values are noted and 'air' refers to $0.48\text{O}_2 + 0.52\text{N}_2$ mixture.

3. Standalone cathode diagnostics

3.1 AMPCAT operating principle

The plasma mechanisms typically described in the microwave cathode literature are summarised here to clarify the general AMPCAT operating principle. Ion current collection through the plasma sheath at the internal cathode surfaces is modelled according to the Child-Langmuir law, since a large potential drop (relative to the bulk neutraliser plasma) drives ion motion at the walls. The ion current density is calculated via:

$$J_i = n_i e v = n_i e \left(\frac{2e(\phi_0 - \phi)}{M} \right)^{1/2} = \frac{4\epsilon_0}{9} \left(\frac{2e}{M} \right)^{1/2} \frac{V^{3/2}}{d^2} \quad (1)$$

where n_i is the ion density, e is the electron charge, v_i is the ion velocity at the wall, $\phi_0 - \phi = V$ is the potential drop through the sheath, M is the ion mass and d is the sheath thickness. The ion and electron densities are typically assumed approximately equal ($n_e \approx n_i$) based on charge quasi-neutrality. The transmission of microwaves into the plasma is limited by the plasma frequency ω_p , since waves with frequency $f > \omega_p$ are reflected at the plasma surface and become evanescent, thus unable to propagate through the bulk plasma. The plasma frequency depends on n_e , which therefore defines a maximum cut-off plasma density n_c for which a given wave frequency is transmitted. This relation is found via:

$$\omega_p = \left(\frac{n_e e^2}{m \epsilon_0} \right)^{1/2} \rightarrow n_c = \frac{m \epsilon_0 (2\pi f)^2}{e^2} \quad (2)$$

where ϵ_0 is the vacuum permittivity and m is the electron mass. A cut-off density $n_c = 7.4 \times 10^{16} m^{-3}$ therefore exists for the $f = 2.45 GHz$ microwave frequency. Despite this, observations in literature consistently record an over-dense bulk plasma for microwave cathodes with an antenna immersed into the plasma volume.^{12,18} This is due to direct heating of electrons in the immediate antenna vicinity, with the extent of this region approximated by the plasma skin depth δ :

$$\delta = \frac{c}{\left(\omega_p^2 - (2\pi f)^2 \right)^{1/2}} \quad (3)$$

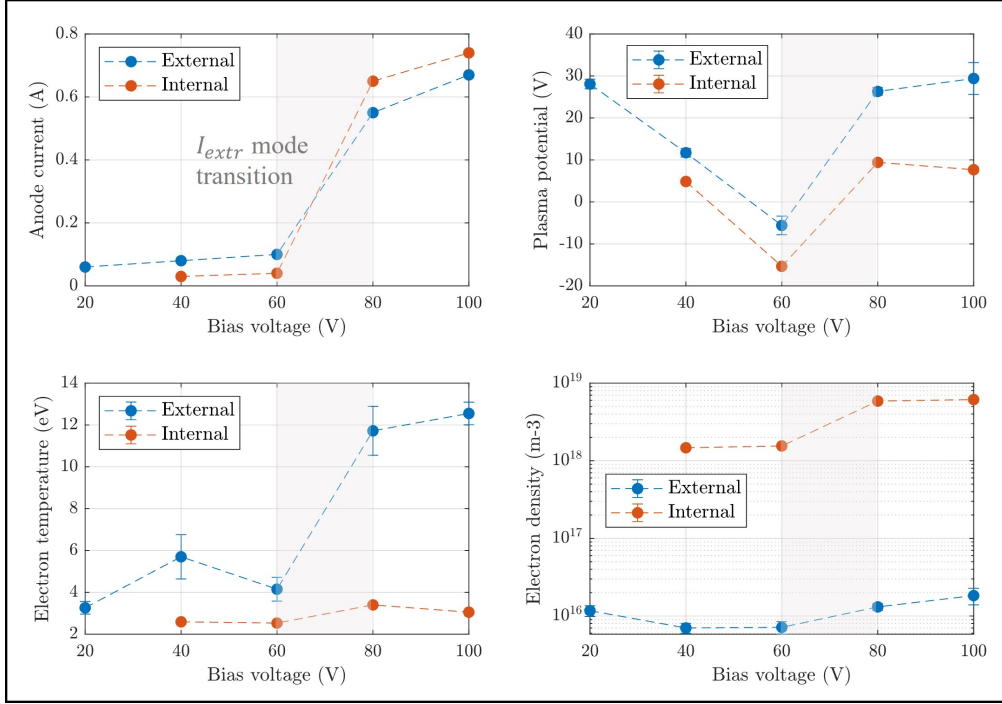
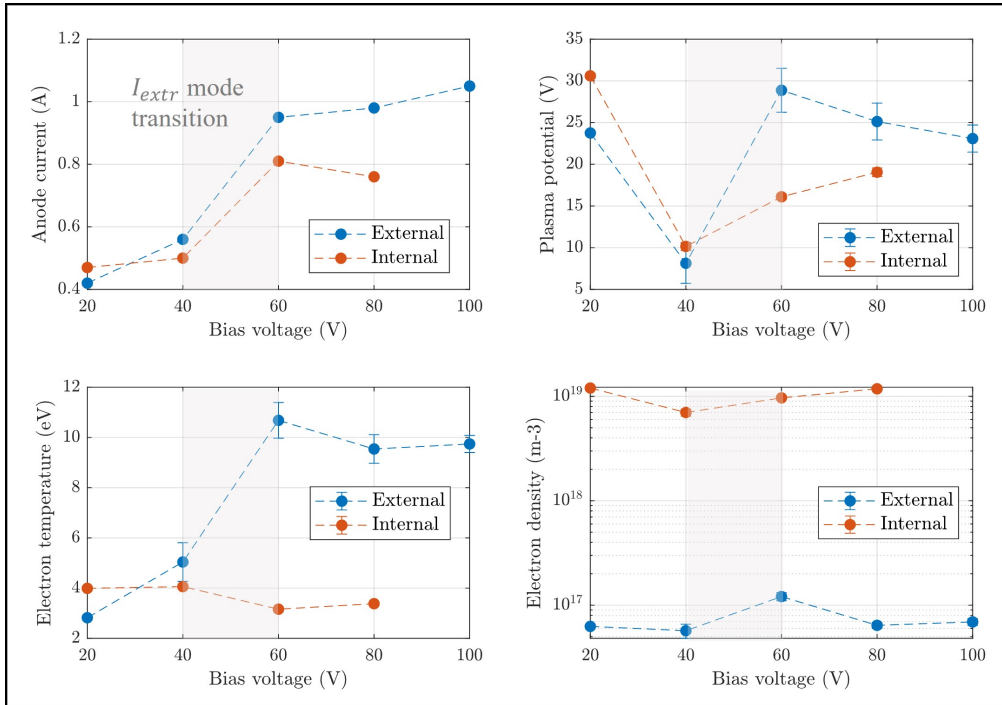
where c is the speed of light. A value of $n_e = 10^{18} m^{-3}$ for instance, in the order typically observed for microwave cathodes, predicts a $\delta = 5.5 mm$ thick layer around the antenna in which coupling of microwave energy into the plasma primarily takes place. Since microwaves do not penetrate far into the over-dense bulk plasma, the diffusion of high-energy electrons from the antenna vicinity supports electron-neutral ionisation collisions throughout the cathode volume. It is likely that electron extraction through the orifice creates a high density of electrons around the antenna tip, given their proximity, forming a virtual cathode which increases microwave-electron energy transfer.¹²

It should be noted that the use of air introduces several additional characteristics of the plasma discharge in comparison to conventional noble gas propellants, such as xenon. The molecular nature of oxygen and nitrogen input to the cathode adds excitation modes, such as vibrational and rotational, for the neutral molecules, thus depleting the energy of the electron population which would otherwise be available for ionisation. For electron-neutral collisions in the case of O_2 and N_2 , the dissociation energies are $5.11 eV$ and $9.76 eV$ respectively,^{3,10} resulting in the production of two atomic particles for every molecule experiencing a collision with a sufficiently high-energy electron. These values are significantly lower than the first ionisation energies for O and N of $13.62 eV$ and $14.53 eV$ respectively,^{28,29} which suggests a predominantly atomic (rather than molecular) ion population. The electronegative nature of oxygen yields the possibility of forming negative ions, unlike xenon, meaning that O^- ions could contribute to the negative cathode extracted current. One mechanism for O^- formation is dissociative electron-attachment reactions with oxygen neutrals, such as: $e^- + O_2 \rightarrow O^- + O$. However, electron-neutral collisions for air species are significantly more likely to result in ionisation events that form positive ions in a stable (non-pulsed) plasma discharge, so any O^- fraction in I_{extr} is expected to be small. For instance Taploo et al³⁹ find a positive oxygen ion production rate $\sim 10^2$ larger at $T_e = 10 eV$, which is representative of the higher-energy electron population which supports ionisation in the AMPCAT.

3.2 AMPCAT plasma properties

As noted earlier, the AMPCAT displays a dual-current behaviour for both air and xenon, whereby a sharp transition to a higher extracted current occurs at a certain high voltage bias value. This transition is visualised by the shading in the plot of anode current against V_b , which is the upper left segment in both Figures 8a and 8b. The maximum extracted current with xenon is typically 30 – 40% higher than air and the transition occurs at lower V_b values. These differences

NEUTRALISER FOR AIR-BREATHING ELECTRIC PROPULSION

(a) $0.48\text{O}_2+0.52\text{N}_2$ propellant.

(b) Xenon propellant.

Figure 8: External and internal plasma properties of AMPCAT with V_b , obtained from Langmuir probe measurements in standalone testing at $\dot{m}_c = 0.1\text{mg/s}$ and $P_{in} = 70\text{W}$.

are explained by a higher degree of ionisation resulting from electron-neutral collisions in the case of xenon. The first ionisation energy of 12.13eV is lower than for oxygen or nitrogen (13.62eV and 14.53eV respectively) and the electron-neutral collision cross-section for xenon is significantly higher. For a $T_e = 15\text{eV}$ electron energy, sufficient for ionisation of all three species, the electron-impact cross-sections for O, N and Xe are $1.28 \times 10^{-21}\text{m}^{-3}$, $1.10 \times 10^{-21}\text{m}^{-3}$ and $1.15 \times 10^{-20}\text{m}^{-3}$ respectively.^{4,16,34} While the thermal velocity of air neutrals is higher than xenon due to a lower molecular mass, this benefit to the global ionisation collision frequency does not overcome the cross-sectional

NEUTRALISER FOR AIR-BREATHING ELECTRIC PROPULSION

Table 1: External plasma parameters for AMPCAT and hollow cathode in standalone testing with $\dot{m}_c = 0.1\text{mg/s}$, from Langmuir probe data. $V_{c/k}$ refers to negative chamber bias for AMPCAT and keeper bias for hollow cathode.

Cathode & propellant	I_{extr} (A)	P_{tot} (W)	V_a (V)	$V_{c/k}$ (V)	V_s (V)	T_e (eV)	n_e (m^{-3})
AMPCAT, air, $P_{in} = 70\text{W}$	0.55	114.0	+20	-60	26.3 ± 0.9	11.7 ± 1.2	$1.3 \pm 0.1 \times 10^{16}$
AMPCAT, Xe, $P_{in} = 70\text{W}$	0.98	148.4	+20	-60	25.1 ± 2.2	9.5 ± 0.6	$6.4 \pm 0.4 \times 10^{16}$
Hollow cathode, Xe	1.00	66.0	+40	+26	7.8 ± 0.8	6.4 ± 0.3	$4.4 \pm 0.2 \times 10^{16}$

difference and the additional electron energy loss mechanisms that exist for air molecules.

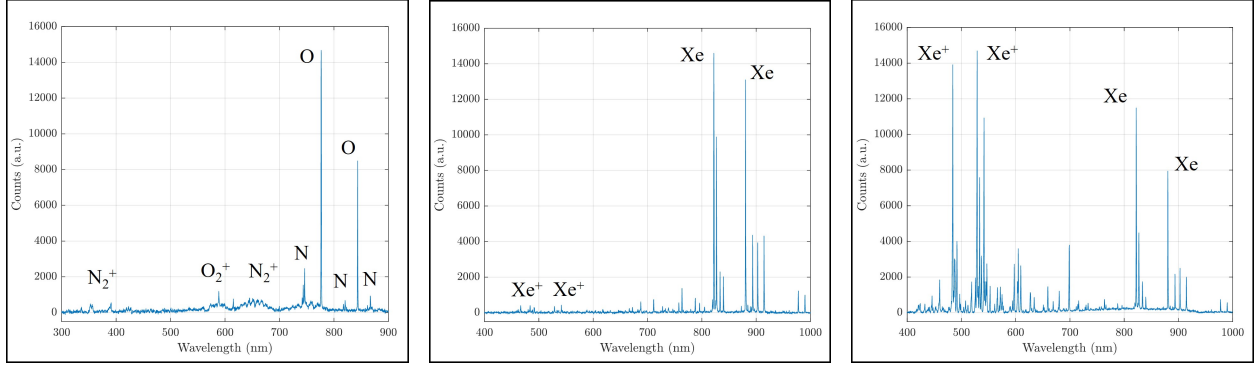
The observed voltage-dependent dual-current behaviour suggests a change in the primary electron emission mechanism within the AMPCAT plasma, triggered at a threshold V_b value. A likely explanation is secondary electron emission (SEE), whereby electrons are emitted from the surface walls from collisions of high energy plasma species. It is therefore supposed that a threshold value of negative bias is required to achieve sufficient ion acceleration through the wall sheath, triggering an avalanche of SEE electrons accelerated into the bulk plasma. This supports a significantly increased level of ionisation through electron-neutral collisions and so results in a transition to the higher-current mode. The internal and external plasma measurements shown in Figures 8a and 8b provide some detail on the behaviour around transition:

- The plasma potential initially decreases with V_b , since the total relative bias is increased by applying a more negative voltage (V_c) to the AMPCAT chamber. The current transition is accompanied by a sharp rise and plateau in V_s , indicating a change to a noticeably different plasma mode.
- The external potential rise supports much higher electron acceleration through the orifice and towards the anode, which is shown by a large increase in external electron temperature. The $\sim 20\text{V}$ difference in V_s between the internal and external plasma drives electron extraction out of the AMPCAT. Internally, the global T_e remains much more constant despite the increased V_s , likely because of a higher density and so more collisional internal plasma. Its value is in a similar range to that recorded by Onodera et al for the $\mu 10$ neutraliser.³¹
- The electron density is found to be around two orders higher in the internal plasma. The current transition corresponds to an increase in n_e both inside and outside the cathode, particularly strong internally in the case of air which explains the sharper I_{extr} profile and indicates a much more ionised plasma.

3.3 Standalone diagnostics comparison with hollow cathode

The external Langmuir probe measurement of the hollow cathode, in a similar standalone setup, allows an analysis of its discharge characteristics at the same $\dot{m}_c = 0.1\text{mg/s}$ xenon flow rate. The anode bias (V_a) is increased at a constant keeper current of 2.5A , which results in a linearly decreasing keeper voltage (V_k) required to sustain the I_k value. The I_{extr} collected on the anode is similarly linear. As in the AMPCAT discharge, the behaviour of V_s and T_e is related, with a saturation in both occurring after $V_a = 35\text{V}$. With regards to the possible differences in thruster-coupling, a comparison of AMPCAT and hollow cathode external plasma properties is shown in Table 1. The bias of the external orifice surface is V_c for the AMPCAT and V_k for the hollow cathode. A similar I_{extr} is chosen to match the cathodes' operation on xenon, which highlights the significantly lower total power (P_{tot}) needed for the hollow cathode. While the electron density is similar between the cathodes for xenon, a key difference is a roughly three times higher external V_s for the AMPCAT operating with both xenon and air, yielding a noticeably higher T_e . Given that electron acceleration is proportional to the square root of the accelerating voltage difference, as shown by the velocity substitution in Equation 1, the measured ratios in T_e between the hollow cathode and the AMPCAT of 1.48 and 1.83, with Xe and air respectively, correlate reasonably well to the 1.79 and 1.84 predicted from $T_e \propto (\Delta V_s)^{1/2}$.

The OES spectrum observed when viewing the orifice of the standalone cathodes is shown in Figure 9. For AMPCAT operation with air, the trace indicates a high degree of dissociation in the air plasma since the peaks corresponding to transitions for O and N are significantly higher than the molecular equivalents. For both air and xenon, the AMPCAT emission is dominated by excited neutrals rather than ions, which is unlike the strong presence of Xe^+ lines in the hollow cathode spectrum (Figure 9c). This is likely caused by the more effective retention of ions within the AMPCAT volume due to the negative internal bias. Ion bombardment clearly occurs to sustain plasma-heating of the emitter in the hollow cathode, however the OES spectrum suggests there is a lower barrier to ion emission in the hollow cathode and so a higher ion population in the discharge.

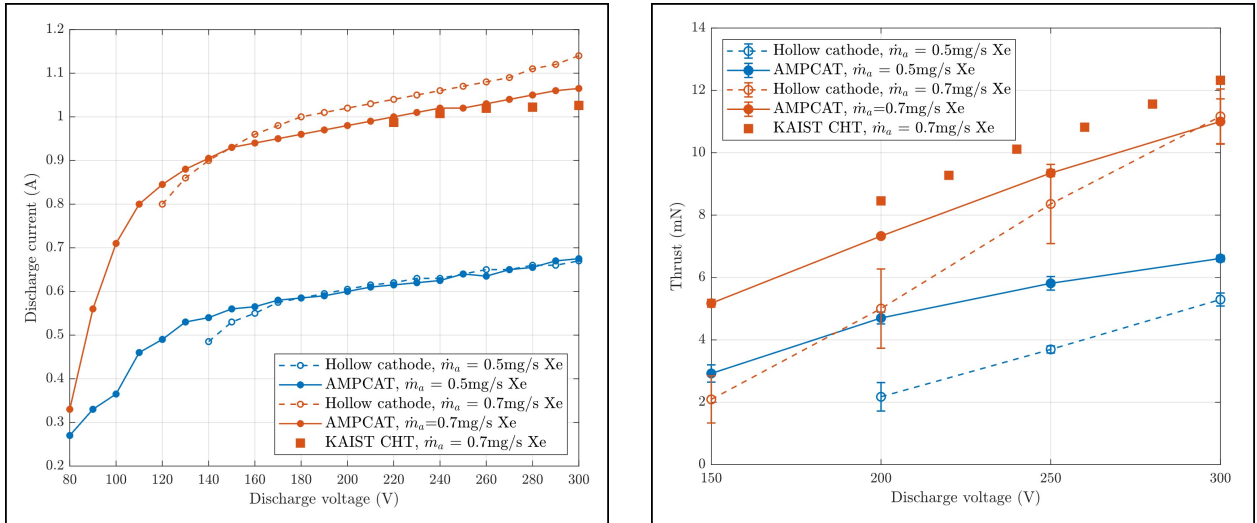


(a) AMPCAT with $I_{extr} = 0.74A$, $P_{in} = 70W$ and $0.48O_2+0.52N_2$. (b) AMPCAT with $I_{extr} = 0.82A$, $P_{in} = 70W$ and Xe. (c) Hollow cathode with $I_{extr} = 0.73A$, $I_k = 2.5A$ and Xe.

Figure 9: OES spectrum of AMPCAT and hollow cathode orifices in standalone testing, at $\dot{m}_c = 0.1mg/s$.

4. Coupled thruster performance

4.1 AMPCAT and hollow cathode comparison



(a) Discharge current with discharge voltage.

(b) Thrust with discharge voltage.

Figure 10: CHT-coupled performance comparison of AMPCAT and hollow cathode running on Xe. For AMPCAT: $P_{in} = 74W$, $V_c = -50V$, and for hollow cathode: $I_k = 2.5A$. Data for KAIST CHT from Kim et al²² also presented as reference, using hollow cathode with $\dot{m}_c = 0.1mg/s$ Xe and $I_k = 1.6A$.

The CHT performance is first investigated with solely xenon, to allow a comparison of the AMPCAT and hollow cathode. The thruster discharge current with discharge voltage (V_d , voltage applied to the anode) is presented in Figure 10a, which shows an approximately flat current profile beyond a given V_d that is characteristic of Hall-type thrusters. The current profile demonstrates a high degree of similarity between the AMPCAT and hollow cathode, particularly for the reduced $\dot{m} = 0.5mg/s$ flow rate. The current data presented by Kim et al²² for the comparable CHT developed at KAIST is also included as a reference. The measured thrust is shown in Figure 10b, which together with the current data indicates close agreement with the KAIST CHT, since the behaviour of both curves is equivalent and the thrust at high V_d is within $1mN$ of the value for both cathodes. This suggests the CHT is representative of the general performance in literature at this low power level. Notably, despite similar I_d (within $40mA$ at $V_d = 200V$), there is a significantly higher thrust for the AMPCAT than for the hollow cathode at low discharge voltages, and this is amplified for the lower $\dot{m}_a = 0.5mg/s$ flow rate. For instance, F_T is more than two times higher for AMPCAT at $V_d = 200V$, though the discrepancy is reduced at higher discharge voltages. This observation of increased relative microwave cathode

NEUTRALISER FOR AIR-BREATHING ELECTRIC PROPULSION

Table 2: Comparison of AMPCAT and hollow cathode parameters in CHT-coupled testing at $\dot{m}_a = 0.5\text{mg/s}$. $I_{k,c}$ refers to keeper current for hollow cathode and internal collected ion current for AMPCAT. I_c values approximately match to allow representative comparison between AMPCAT operation on air and Xe, for $V_{cg} \approx 0\text{V}$ and so $I_c \approx I_d$.

Cathode parameters	Propellant	$I_{k,c}$ (A)	V_{cg} (V)	C_e (W/A)
Hollow cathode	0.1 mg/s, Xe	2.51	-24.0	32.4
AMPCAT, $P_{in} - Pr = 34\text{W}$, $V_c = -30\text{V}$	0.1 mg/s, Xe	0.69	0	79.3
AMPCAT, $P_{in} - Pr = 54\text{W}$, $V_c = -100\text{V}$	0.1 mg/s, air	0.61	2.5	143.4

performance at low I_d resembles the findings of Morishita et al.²⁷ In this study, the coupled anode performance values at $V_d = 300\text{V}$ and $\dot{m}_a = 0.5\text{mg/s}$ are: $P_d = 202\text{W}$, $F_T = 6.6\text{mN}$, $I_{sp} = 1370\text{s}$ and $\eta_T = 0.22$.

The cathode to ground voltage behaviour is found to be inverse to the I_d vs V_d curve for both cathodes, i.e. dropping with discharge voltage, and settling to roughly 19V for the AMPCAT and around -24V for the hollow cathode at $\dot{m}_a = 0.5\text{mg/s}$. V_{cg} decreases for larger anode flow rates due to a larger I_d , and therefore a steeper potential gradient required to support the increased cathode electron current to the thruster discharge.¹⁷ Unsurprisingly, this also occurs when decreasing the AMPCAT power and negative bias, since electron emission of the cathode itself is reduced. V_{cg} is seen to drop linearly with P_{in} , while for a reduction in V_c it is initially stable until a threshold bias, below which it similarly decreases in a linear manner. A positive AMPCAT cathode to ground voltage is recorded when the internal collected ion current is larger than I_d , falling to 0V when $|I_i| = I_d$ and becoming negative when I_i is insufficient to balance I_d . This is explained from an ion beam neutralisation perspective in regards to the grounded walls of the vacuum chamber, since the AMPCAT: a) floats above the chamber when the required neutralisation current is less than I_{extr} , and b) conversely floats below the chamber ground when the $|I_i| - I_d$ margin disappears and an increased current for neutralisation must be drawn from the cathode. Notably, a reduction in AMPCAT P_{in} and V_c does not significantly affect the discharge current or thrust. Therefore, the input microwave power and negative bias can be reduced to 39W and -30V respectively for $\dot{m}_a = 0.5\text{mg/s}$ without prompting a negative V_{cg} across the V_d range. Using this case, a comparison of the cathode performance metrics is shown in Table 2. Here the electron production cost (C_e) is calculated for the AMPCAT as:

$$C_e = \frac{I_c|V_c| + (P_{in} - P_r)}{I_c} \quad (4)$$

where P_r is the reflected microwave power. This therefore reduces to $C_e = V_k$ for the hollow cathode. An AMPCAT power cost with xenon around 2.5 times higher than the hollow cathode is comparable with literature at these discharge current values.^{23,27} An approximately 1.7 times increase in I_{extr} is observed for the AMPCAT with xenon between standalone and thruster-coupled ($V_d = 200\text{V}$, $\dot{m}_a = 0.5\text{mg/s}$) testing, at equivalent V_c and P_{in} values.

4.2 Comparison of air and xenon as AMPCAT propellant

The thruster performance comparison between AMPCAT operation on xenon and the $0.48\text{O}_2 + 0.52\text{N}_2$ mixture is shown in Figures 11a and 11b, for an equivalent cathode microwave power and internal bias. A fast thruster discharge ignition is achieved in the same way for AMPCAT operation on air as for xenon, since the cathode produces current (at a given \dot{m}_c and V_c) as soon as microwave power is applied, and the thruster is found to operate in an equivalent and stable manner. A $\sim 0.2\text{A}$ higher discharge current is measured for air, however (at least at $V_d = 200\text{V}$) the thrust is also 0.6mN higher, resulting in similar anode η_T values of 19.3% and 18.6% for xenon and air respectively. The observed similar level of CHT current and thrust when switching to air as AMPCAT propellant goes some way to validating the air-breathing cathode, at least at this low $P_d = 113 - 268\text{W}$ range where the I_{extr} available with air is sufficient to support thruster operation. As shown in Table 2, the power cost of using air is found to be around 1.8 times higher than for xenon. In other words, the AMPCAT DC and microwave power can be significantly reduced for an equivalent discharge current (and cathode to ground voltage) when operating with xenon.

5. Coupled discharge diagnostics

5.1 Near-field plasma parameters

The plasma properties in the thruster near-field are measured using fixed Langmuir probes. Such a setup includes a probe halfway between the cathode orifice and the thruster axis ($r = r_{cat}/2$, $z = z_{cat}$), with a second probe symmetrically

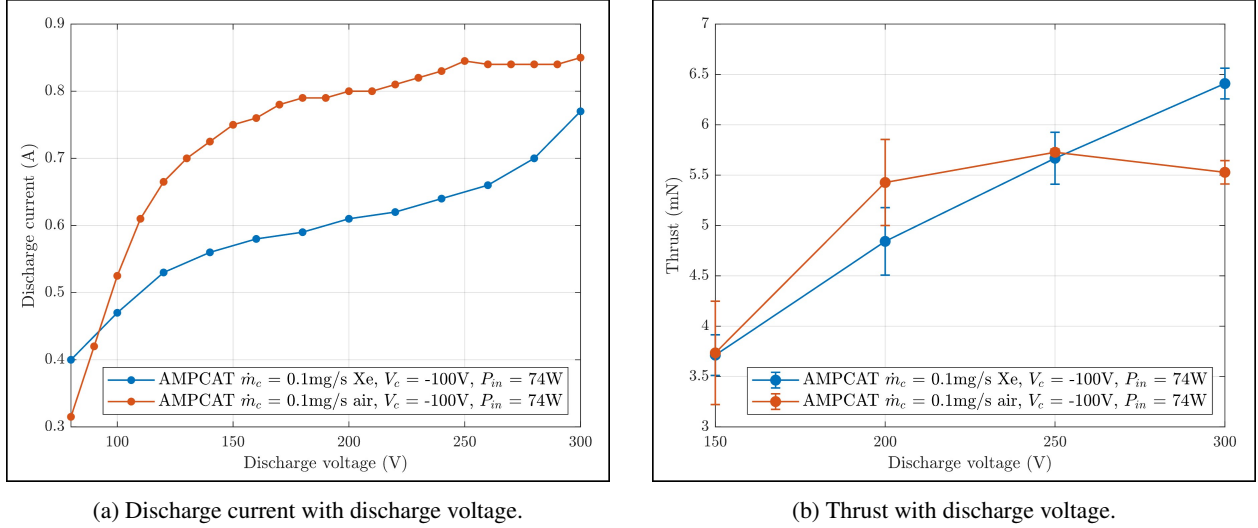


Figure 11: CHT-coupled performance comparison of AMPCAT operating on Xe and air, for CHT $\dot{m}_a = 0.5 \text{ mg/s Xe}$.

Table 3: Comparison of V_s , T_e and n_e between hollow cathode with Xe and AMPCAT operating on both Xe and air, for $\dot{m}_a = 0.5 \text{ mg/s}$, $V_d = 150 \text{ V}$. Data originates from Langmuir probes at halfway to cathode orifice radius on ‘near-cathode’ ($r = r_{cat}/2 = 32 \text{ mm}$) and ‘cathode-opposite’ ($r = -r_{cat}/2 = -32 \text{ mm}$) sides of ion plume, at cathode axial position ($z = z_{cat} = 40 \text{ mm} = 0.8TD$).

	Hollow cathode, $\dot{m}_c = 0.1 \text{ mg/s Xe}$			AMPCAT, $\dot{m}_c = 0.1 \text{ mg/s Xe}$			AMPCAT, $\dot{m}_c = 0.1 \text{ mg/s air}$		
	V_s (V)	T_e (eV)	n_e (m^{-3})	V_s (V)	T_e (eV)	n_e (m^{-3})	V_s (V)	T_e (eV)	n_e (m^{-3})
$r_{cat}/2$	70.7	12.1	3.7×10^{17}	32.3	8.7	5.0×10^{17}	65.3	14.9	2.7×10^{17}
	± 5.7	± 1.3	± 0.5	± 3.2	± 0.8	± 0.6	± 7.3	± 1.6	± 0.4
$-r_{cat}/2$	68.7	11.9	4.0×10^{17}	40.9	11.9	2.2×10^{17}	64.8	13.4	3.9×10^{17}
	± 3.2	± 0.7	± 0.3	± 3.8	± 0.8	± 0.3	± 3.7	± 0.6	± 0.4

on the opposite (non-cathode) side of the thruster plume. These measurements are presented in Table 3, comparing the hollow cathode to AMPCAT with air and xenon at a low 150V discharge voltage. The most notable difference is a roughly 30–40V lower plasma potential for the AMPCAT with xenon compared to the hollow cathode, which suggests a significantly improved electron transport into the CHT discharge for the AMPCAT and thus a smaller V_s needed in the cathode vicinity to draw sufficient electron current into the ion plume. This V_s difference provides an explanation for the improved thrust with the AMPCAT at low V_d in comparison to the hollow cathode baseline, possibly through:

- A reduced radial E-field yielding less divergence of the ion beam and therefore an increased thrust, as noted by Sommerville et al^{37,38} when moving the cathode to improve electron mobility into the discharge.
- Better coupling of the cathode electron current to the CHT discharge resulting in more upstream ionisation within the discharge channel, as suggested by Raitses et al,³³ allowing ion acceleration through a larger voltage drop.

It is possible that a more numerous higher-energy electron population in the AMPCAT discharge (shown by the larger standalone T_e in Table 1) is effective in establishing an improved coupling of I_{extr} with the thruster plume, yielding a higher n_e than for the hollow cathode and a lower required V_s in the CHT near-field. Relative to xenon, the increased T_e but reduced n_e values for AMPCAT with air are explained by a simultaneously lighter propellant mass and lower degree of ionisation of the cathode plasma, closely matching the standalone data in Table 1.

An initial suggestion for the lower V_s in the AMPCAT vicinity with xenon is that the negative bias applied to the plasma chamber of the microwave cathode affects the thruster discharge. However, this is not supported by the performance tests, which observe an equivalent I_d and F_T for AMPCAT V_c variation between -100 V and -30 V (with sufficient P_{in}). This is also shown in Figure 12, which depicts a similar axial variation in V_s for different P_{in} and V_c . The cathode orifice is located at $z = 40 \text{ mm}$. The plot shows a generally linear decrease in plasma potential with distance to

NEUTRALISER FOR AIR-BREATHING ELECTRIC PROPULSION

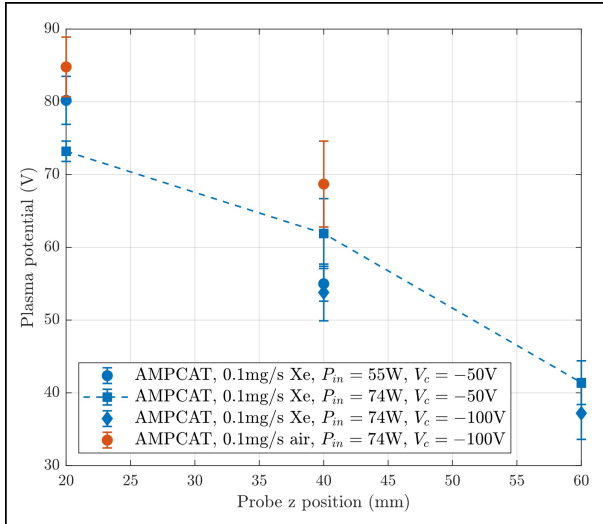


Figure 12: Axial variation of V_s along thruster axis between air and Xe as AMPCAT propellant, for $\dot{m}_a = 0.5\text{mg/s}$, $V_d = 150\text{V}$.

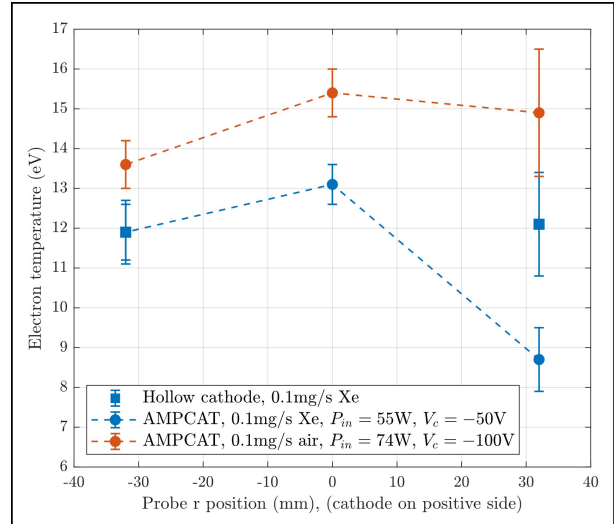


Figure 13: Radial variation of T_e at cathode axial position ($z = z_{cat}$) between hollow cathode and AMPCAT, for $\dot{m}_a = 0.5\text{mg/s}$, $V_d = 150\text{V}$.

the thruster exit and implies that a significant amount of ion acceleration occurs outside the CHT channel at these low $V_d = 150\text{V}$ and $\dot{m}_a = 0.5\text{mg/s}$ values, since the $V_s \sim 75\text{V}$ at $z = 20\text{mm}$ is roughly half the total anode voltage. This external acceleration is also measured by Smirnov et al³⁶ for a low-power CHT. The $\sim 10\text{V}$ higher axial potential with air is likely related to an increased radial E-field required to maintain cathode electron current extraction (see Table 3). Figure 13 visualises the reduced symmetry in across-plume plasma properties for AMPCAT operation with both air and xenon than for the hollow cathode. It is likely that the higher T_e observed for air is effective at boosting ionisation in the CHT at low discharge voltages, and so I_d and F_T , explaining the behaviour seen in Figure 11.

5.2 Far-field plasma parameters

Figure 14 shows the variation of ion current density (J_i) with angle of the Faraday probe away from the thruster axis, defined as 0° . Integration of J_i shows that the plume divergence is extremely similar for the hollow cathode and AMPCAT operation on xenon and air at this $\dot{m}_a = 0.5\text{mg/s}$, $V_d = 150\text{V}$ condition, since the 90% half-angle differs by only 1° . This implies that increased divergence from a strong radial E-field, suggested as a by-product of

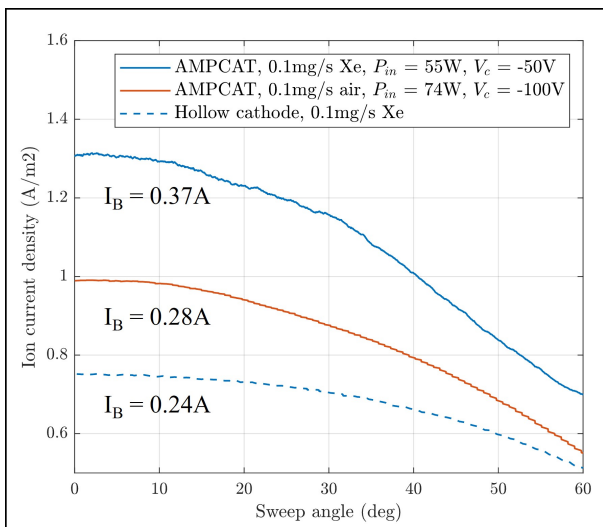


Figure 14: Angular variation of J_i from Faraday probe, for $\dot{m}_a = 0.5\text{mg/s}$, $V_d = 150\text{V}$. Thruster axis is at 0° .

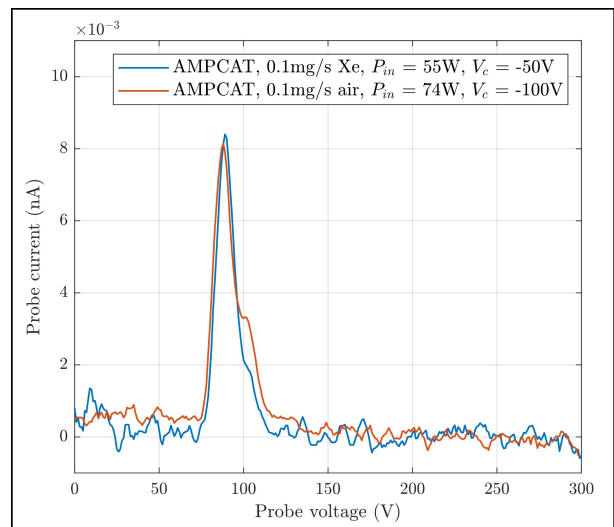


Figure 15: Wien filter current with probe voltage, for $\dot{m}_a = 0.5\text{mg/s}$, $V_d = 150\text{V}$.

poor cathode current coupling in the above, is not a significant performance loss mechanism, at least at $V_d = 150V$. However, a significant difference is observed in the total beam current (I_B), as labelled in the figure, from which the current utilisation efficiency (η_B) can be calculated as the ratio to the discharge current: $\eta_B = I_B/I_d$. This yields similar η_B values of 0.39 and 0.42 for the hollow cathode and AMPCAT with air, while $\eta_B = 0.55$ is notably higher for the AMPCAT operating on xenon. It is useful to consider the current utilisation efficiency values alongside the (anode) mass utilisation, which quantifies the beam current generated from a given anode propellant flow: $\eta_m = I_B M / e \dot{m}_a$. The η_m values are found as 0.65 for the hollow cathode, 0.77 for AMPCAT with air and 1.00 for the AMPCAT with xenon. Together, these utilisation efficiencies imply:

- For xenon, the AMPCAT achieves both increased ionisation and improved ion acceleration over the hollow cathode at low discharge voltages.
- Relative to the hollow cathode, the AMPCAT with air likely supports a similar level of ion acceleration, since the η_B values are close, however improved ionisation in the CHT is indicated by a noticeably higher η_m , yielding a higher discharge power and thrust at low V_d .

The high $\eta_m = 1.00$ for AMPCAT with xenon is commonly observed in CHT literature (see Section 1) and explained by a non-negligible fraction of multiply-charged species in the ion beam. At this low $V_d = 150V$, this is not observed in Wien filter measurements, as shown in Figure 15. Here, only the singly-ionised Xe^+ peak is visible, although Xe^{2+} and Xe^{3+} peaks are observed for higher discharge voltages, so it is likely that in this case a small doubly-charged Xe peak is obscured by the probe noise. This data shows a similar peak ion velocity for both air and xenon through the AMPCAT, however a higher V_s measured at the Wien filter for air means that the effective beam voltage is smaller. Taking this into account, V_B is calculated as 79.2V for AMPCAT operation on xenon and 69.2V with air, from which the voltage utilisation efficiency (η_v) is found via: $\eta_v = V_B/V_d$. Low values for both cathode propellants, of $\eta_v = 0.53$ and 0.46 for Xe and air respectively, indicate that higher discharge voltages are required for a more representative level of ion acceleration in the CHT. Notably, the Wien filter trace shows a high-energy tail in the Xe^+ ion population for the AMPCAT running on air and xenon. It is possible that this indicates that AMPCAT operation on both propellants provides electrons energetic enough to ionise a component of the neutral population closer to the anode, thus boosting their acceleration and so the total thrust value.

6. Conclusions

In summary, the Air-Breathing Microwave CATHode (AMPCAT), operating on both air and xenon, is compared to a conventional hollow cathode. In standalone testing, the observed transition to a higher-current mode in the AMPCAT with air is found to correspond with a significant increase in external electron temperature and internal electron density. The standalone AMPCAT discharge therefore exhibits a notably higher T_e than the hollow cathode, driven by a correspondingly increased plasma potential. Both cathodes are coupled with a cylindrical Hall thruster (CHT), which demonstrates a matching discharge current profile but increased performance for the AMPCAT when operating on xenon, particularly at low discharge voltages. Near-field Langmuir probe measurements reveal a 30 – 40V lower V_s around the cathode axial position for the AMPCAT, indicating an improved mobility of cathode electrons into the thruster discharge than for the hollow cathode, and this is supported by beam current measurements suggesting improved ionisation and ion acceleration. The CHT is successfully coupled with the AMPCAT operating on air, with an equivalent thrust to xenon at low discharge voltages, though at a higher discharge current and cathode power. It is suggested the increased temperature of the electron and ion population in the thruster plume with the AMPCAT, based on Langmuir probe and Wien filter data, may support more upstream ionisation in the CHT channel and so a higher level of ion acceleration.

Acknowledgments

The authors would like to thank the Propulsion Lab Technical Support and Mechanical Engineering Workshop teams at Surrey, particularly Brian Eades for his skillful machining of cathode components. M. Tisaev thanks the Doctoral College of the University of Surrey for his PhD scholarship funding.

References

- [1] M. Ahmed, B. Karadag, S. Masillo, and A. Lucca Fabris. Development of a modular hollow cathode for ground testing of plasma thrusters. Submitted for publication to *Journal of Vacuum*, 2023.
- [2] T. Andreussi et al. The aether project: development of air-breathing electric propulsion for vleo missions. *CEAS Space Journal*, 2022.
- [3] P. Brix and G. Herzberg. The dissociation energy of oxygen. *The Journal of Chemical Physics*, 21(12):2240–2240, 1953.
- [4] E. Brook, M. Harrison, and A. Smith. Measurements of the electron impact ionisation cross sections of he, c, o and n atoms. *Journal of Physics B: Atomic and Molecular Physics*, 11(17):3115, 1978.
- [5] P. Crandall and R. Wirz. Air-breathing electric propulsion: mission characterization and design analysis. *Journal of Electric Propulsion*, 1(1), 2022.
- [6] N. Crisp et al. The benefits of very low earth orbit for earth observation missions. *Progress in Aerospace Sciences*, 117:100619, 2020.
- [7] J. Cronin. Practical aspects of modern dispenser cathodes. *Microwave Journal*, 1979.
- [8] D. Di Cara, J. Gonzalez del Amo, et al. Ram electric propulsion for low earth orbit operation: an esa study. In *30th International Electric Propulsion Conference, Florence, Italy*, Sep 2007.
- [9] E. Ferrato et al. Development roadmap of sitael’s ram-ep system. In *36th International Electric Propulsion Conference, Vienna, Austria*, 2019.
- [10] D. Frost and C. McDowell. The dissociation energy of the nitrogen molecule. *Proceedings of the Royal Society of London. Mathematical and Physical Sciences*, 236(1205):278–284, 1956.
- [11] K. Fujita. Air intake performance of air breathing ion engines. *J. Japan Soc. Aeronaut. Space Sci.*, 52(610):514–521, 2004.
- [12] I. Funaki and H. Kuninaka. Overdense plasma production in a low-power microwave discharge electron source. *Japanese Journal of Applied Physics*, 40(Part 1, No. 4A):2495–2500, 2001.
- [13] H. Gallagher. Poisoning of lab6 cathodes. *Journal of Applied Physics*, 40(1):44–51, 1969.
- [14] D. Goebel, K. Jameson, and R. Hofer. Hall thruster cathode flow impact on coupling voltage and cathode life. *Journal of Propulsion and Power*, 28(2):355–363, 2012.
- [15] V. Hruby, K. Hohman, and J. Szabo. Air breathing hall effect thruster design studies and experiments. In *37th International Electric Propulsion Conference, Cambridge, USA*, 2022.
- [16] Y. Itikawa and A. Ichimura. Cross sections for collisions of electrons and photons with atomic oxygen. *Journal of Physical and Chemical Reference Data*, 19(3):637–651, 1990.
- [17] K. Jameson, D. Goebel, R. Hofer, and R. Watkins. Cathode coupling in hall thrusters. In *30th International Electric Propulsion Conference, Florence, Italy*, 2007.
- [18] H. Kamhawi, J. Foster, and M. Patterson. Operation of a microwave electron cyclotron resonance cathode. In *40th AIAA Joint Propulsion Conference, Fort Lauderdale*, 2004.
- [19] H. Kawasaki et al. Interim report of super low altitude satellite operation. In *IGARSS 2018 - 2018 IEEE International Geoscience and Remote Sensing Symposium*, pages 4066–4069, 2018.
- [20] H. Kim, W. Choe, Y. Lim, S. Lee, and S. Park. Magnetic field configurations on thruster performance in accordance with ion beam characteristics in cylindrical Hall thruster plasmas. *Applied Physics Letters*, 110(11), 2017.
- [21] H. Kim, Y. Lim, W. Choe, S. Park, and J. Seon. Effect of magnetic field configuration on the multiply charged ion and plume characteristics in Hall thruster plasmas. *Applied Physics Letters*, 106(15), 2015.

- [22] H. Kim, Y. Lim, W. Choe, and J. Seon. Effect of multiply charged ions on the performance and beam characteristics in annular and cylindrical type Hall thruster plasmas. *Applied Physics Letters*, 105(14), 2014.
- [23] H. Kuninaka and K. Nishiyama. Development of 20cm diameter microwave discharge ion engine system $\mu 20$. In *39th AIAA/ASME/SAE/ASEE Joint Propulsion Conference and Exhibit*, 2003.
- [24] S. Masillo, A. Lucca Fabris, B. Karadag, T. Potterton, A. Knoll, and P. Bianco. Experimental characterisation of the novel halo plasma thruster for small satellite applications. In *SPACE PROPULSION 2020+1, Online*, 2021.
- [25] S. Masillo, J. Stubbing, K. Swar, D. Staab, A. Garbayo, and A. Lucca Fabris. Validation of a torsional balance for thrust measurements of hall effect and microwave-based space propulsion systems. *Review of Scientific Instruments*, 93(11), 2022.
- [26] T. Morishita, R. Tsukizaki, S. Morita, D. Koda, K. Nishiyama, and H. Kuninaka. Effect of nozzle magnetic field on microwave discharge cathode performance. *Acta Astronautica*, 165:25–31, 2019.
- [27] T. Morishita, R. Tsukizaki, N. Yamamoto, K. Kinefuchi, and K. Nishiyama. Application of a microwave cathode to a 200-w hall thruster with comparison to a hollow cathode. *Acta Astronautica*, 176:413–423, 2020.
- [28] National Institute of Standards and Technology. *Basic atomic spectroscopic data: N*, Jun 2023.
- [29] National Institute of Standards and Technology. *Basic atomic spectroscopic data: O*, Jun 2023.
- [30] K. Nishiyama. Air breathing ion engine. In *Proc. of 24th International Symposium on Space Technology and Science, Miyazaki, Japan*, 2004.
- [31] N. Onodera et al. Electron emission mechanism of microwave discharge neutralizer. In *26th International Electric Propulsion Conference, Kitakyushu, Japan*, 1999.
- [32] Y. Raitses and N. Fisch. Parametric investigations of a nonconventional Hall thruster. *Physics of Plasmas*, 8(5):2579–2586, 2001.
- [33] Y. Raitses, A. Smirnov, and N. Fisch. Enhanced performance of cylindrical Hall thrusters. *Applied Physics Letters*, 90(22), 2007.
- [34] D. Rapp and P. Englander-Golden. Total cross sections for ionization and attachment in gases by electron impact. i. positive ionization. *The Journal of Chemical Physics*, 43(5):1464–1479, 1965.
- [35] A. Shirasaki and H. Tahara. Operational characteristics and plasma measurements in cylindrical Hall thrusters. *Journal of Applied Physics*, 101(7), 2007.
- [36] A. Smirnov, Y. Raitses, and N. Fisch. Controlling the plasma flow in the miniaturized cylindrical hall thruster. *IEEE Transactions on Plasma Science*, 36(5):1998–2003, 2008.
- [37] J. Sommerville and L. King. Hall-effect thruster–cathode coupling, part i: Efficiency improvements from an extended outer pole. *Journal of Propulsion and Power*, 27(4):744–753, 2011.
- [38] J. Sommerville and L. King. Hall-effect thruster–cathode coupling, part ii: Ion beam and near-field plume. *Journal of Propulsion and Power*, 27(4):754–767, 2011.
- [39] A. Taploo, L. Lin, and M. Keidar. Analysis of ionization in air-breathing plasma thruster. *Physics of Plasmas*, 28(9), 2021.
- [40] M. Tisaev, E. Ferrato, V. Giannetti, C. Paissoni, N. Baresi, A. Lucca Fabris, and T. Andreussi. Air-breathing electric propulsion: Flight envelope identification and development of control for long-term orbital stability. *Acta Astronautica*, 191:374–393, 2022.
- [41] M. Tisaev, B. Karadag, E. Ferrato, A. Kitaeva, T. Andreussi, and A. Lucca Fabris. Development of an air-breathing neutraliser as part of the aether system. In *37th International Electric Propulsion Conference, Cambridge, USA*, 2022.
- [42] T. Wantock. *Thrust balance performance characterisation and internal langmuir probe plasma diagnostics for a halo thruster*. PhD thesis, Surrey Space Centre, University of Surrey, 2018.